Applied Surface Science 425 (2017) 272–281

Contents lists available at ScienceDirect

Applied Surface Science

journal homepage: www.elsevier.com/locate/apsusc

Full Length Article

Synthesis and properties of a high-capacity iron oxide adsorbent for fluoride removal from drinking water

Chang Zhang, Yingzhen Li, Ting-Jie Wang*, Yanping Jiang, Jason Fok

Department of Chemical Engineering, Tsinghua University, 100084, Beijing, China

ARTICLE INFO

Article history:
Received 17 March 2017
Received in revised form 12 June 2017
Accepted 14 June 2017
Available online 20 June 2017

Keywords:
Adsorbent
Iron oxide
Fluoride removal
Ethanol treatment
Drinking water

ABSTRACT

A novel iron oxide adsorbent with a high fluoride adsorption capacity was prepared by a facile wet-chemical precipitation method and ethanol treatment. The ethanol-treated adsorbent was amorphous and had a high specific surface area. The adsorption capacity of the treated adsorbent was much higher than that of untreated adsorbent. The Langmuir maximum adsorption capacity of the adsorbent prepared at a low final precipitation pH (≤9.0) and treated with ethanol reached 60.8 mg/g. A fast adsorption rate was obtained, and 80% of the adsorption equilibrium capacity was achieved within 2 min. The adsorbent had high fluoride-removal efficiency for water in a wide initial pH range of 3.5–10.3 and had a high affinity for fluoride in the presence of common co-anions. The ethanol treatment resulted in structure transformation of the adsorbent by inhibiting the crystallization of the nano-precipitates. The adsorption was confirmed to be ion exchange between fluoride ions and the hydroxyl groups on the adsorbent surface.

1. Introduction

Excess fluoride in drinking water has been shown to cause serious health problems [1]. The upper limit of fluoride content in drinking water is restricted to 1.5 mg/L according to the WHO guidelines and 1.0 mg/L according to the standards for drinking water quality of China (GB5749-2006) [2]. Groundwater with excess fluoride is widespread all over the world, especially in developing countries like China and India [3,4]. Most cases of endemic fluorosis occur in rural areas of developing countries, where the less-developed economy and technological challenges aggravate the problem of unsafe drinking water. Therefore, an economical and effective method for fluoride removal in drinking water is of great importance [5–7].

Various methods have been developed for fluoride removal, such as precipitation and flocculation [8,9], membrane separation [10–12], electrodialysis [13,14], and adsorption [15–18]. In precipitation and flocculation process, lime and alum are used to form insoluble precipitants with fluoride. The fluoride concentration of the treated solution still remains about 8.0 mg/L due to the solubility of the formed precipitants [8,9]. Membrane separation process mainly contains reverse osmosis and nanofiltration. It can produce water with extremely high purity, but suffers from high energy consumption and membrane fouling [10–12]. In electrodialysis process, fluoride ions transfers through a semipermeable membrane due to an electric potential. It is costly and easily influenced by coexisting ions [13,14]. Among these, adsorption has been considered as the most efficient and applicable method for fluoride removal due to its easy operation, low energy consumption, and stable treatment efficiency [17], making it ideal for use in less-developed rural areas. In recent years, the oxides and hydroxides of different metals, such as Fe [20,21], Al [22], Mg [23,24], Ti [25], Zr [26–29], Ce [30,31], and La [32–34], have been reported as efficient adsorbents for fluoride removal.

Expensive metal oxides like rare earth metal oxides have a significant affinity to fluoride, but the extremely high cost restricts their application. In comparison, iron oxides are more easily available and cost-effective. The affinity of iron oxides for fluoride ions has been confirmed in previous reports [1]. However, the maximum adsorption capacity of iron oxide adsorbents for fluoride is mostly less than 10 mg/g [20,21,35,36], which still needs to be improved to compete with other metal oxide adsorbents. For an identified adsorbent, high specific surface area usually provides more surface active sites for adsorption, affording a high adsorption capacity [5,37–41]. Therefore, high specific surface area is desirable in the preparation of an oxide adsorbent.

Metal oxide adsorbents are usually prepared with a wet-chemical precipitation process [1,19,41–47]. The effects of different

* Corresponding author.
E-mail address: wangtj@tsinghua.edu.cn (T.-J. Wang).

http://dx.doi.org/10.1016/j.apsusc.2017.06.159
0169-4332/

precipitation conditions, such as iron precursor, precipitant, reaction medium, reaction time, reaction temperature, precipitation pH, and adjustment additives, have been discussed in detail in the literature [48–52]. The precipitation process of amorphous iron oxide with a high specific surface area usually needs expensive additives, like surfactant and noble metal ions [21,53,54], resulting in low cost efficiency of the preparation process. For example, Chen et al. added Ti(IV) in the precipitation process of the iron oxide adsorbent. The adsorption capacity increased from 11.6 mg/g to 47.0 mg/g, but the cost of the adsorbent increased by hundreds of times, because Ti(IV) is much more expensive than Fe(II) [39]. Ethanol is known as a good dispersant, and has been used to wash the precipitated metal oxide adsorbents [23,39]. However, ethanol treatment is only used as an auxiliary process in the adsorbent preparation. The effect of the ethanol treatment on the adsorbent properties has rarely been studied.

In this work, the structural transformation of iron oxide caused by the ethanol treatment was studied. The ethanol-treated adsorbent was highly amorphous, had a high specific surface area, and its adsorption capacity was much higher than that of the adsorbent without ethanol treatment. The effects of the final precipitation pH and thermal treatment were investigated to improve the adsorption performance of the ethanol-treated adsorbent. The adsorption mechanism of the adsorbent, adsorption isotherm, and kinetics were studied. The adsorption capacity of the adsorbent at different pH values and different coexisting ions was also investigated.

2. Experiments

2.1. Preparation of the iron oxide adsorbent

The iron oxide adsorbent was prepared by a facile wet-chemical precipitation method. First, 100 mL of 0.9 M $FeSO_4{\cdot}7H_2O$ solution was taken in a flask. Then, 12.5 wt% ammonia was titrated dropwise into the solution under magnetic agitation, until the slurry pH reached a set value, namely, the final precipitation pH. The obtained precipitate was washed three times by centrifugation using deionized water. The washed precipitate was then placed in ethanol, dispersed well by magnetic agitation, and then re-collected by centrifugation. The collected precipitate was dried at 80 °C in an oven for 2 h and subsequently grinded, obtaining the ethanol-treated adsorbent. The adsorbent was then sieved to 30–100 μm for the adsorption performance measurement. For comparison, the adsorbent without ethanol treatment was prepared using the same procedure.

2.2. Investigation of preparation conditions

The effects of the final precipitation pH and thermal treatment on the adsorbent properties were investigated. To examine the effect of the final precipitation pH, 9 mL, 18 mL, 29 mL, and 40 mL ammonia, respectively, was titrated into 100 mL of 0.9 M $FeSO_4{\cdot}7H_2O$ solution, which corresponds to the final precipitation pH of 7.6, 8.0, 9.0, and 9.6, respectively. The procedure used was the same as described in section 2.1.

To investigate the effect of thermal treatment, the ethanol-treated adsorbent with a final precipitation pH of 9.0 was thermally treated in a muffle furnace for 1.5 h at a set temperature of 100 °C, 200 °C, 300 °C, 400 °C, and 500 °C. The properties and adsorption performance of the obtained iron oxide adsorbents were further examined.

2.3. Characterization

The chemical composition and structure of the adsorbent surface were examined by X-ray photoelectron spectroscopy (XPS, PHI Quantera SXM, ULVAC-PHI, Japan). The morphology and microstructure of the adsorbent were examined by scanning electron microscopy (SEM, Carl ZeissMerlin, German) and high resolution transmission electron microscopy (HRTEM, JEM-2011, JEOL Co., Japan), respectively. The crystalline structure of the adsorbent was analyzed using an X-ray diffraction analyzer (XRD, D8-Advance, Brucker, Germany) over the range 5°–90° with Cu Kα radiation at a scan speed of 10°/min. The specific surface area of the adsorbent was measured by nitrogen adsorption using an Autosorb-iQ2-C (Quantachrome Instruments, USA). The surface zeta potential of the adsorbent was measured using a zeta potential instrument (ZetaPALS, Brookhaven Instruments Corporation, USA). The chemical structure of the adsorbent surface before and after defluoridation was examined by Fourier transform infrared spectroscopy (FT-IR, Thermo Nicolet 560, USA).

2.4. Adsorption performance

(1) Adsorption isotherm

The adsorption isotherm of the adsorbent shows the equilibrium fluoride adsorption capacities versus equilibrium fluoride concentrations. The equilibrium adsorption capacity was measured in batch adsorption experiments, as described in our previous work [38]. Fluoride solutions in a concentration range of 5–500 mg/L were prepared by dissolving NaF in deionized water. Then, 50 mg adsorbent was added into a conical flask containing 50 mL fluoride solution. The flask was shaken on a thermostat shaker at 180 rpm and 25 °C for 12 h to ensure the adsorption equilibrium. After equilibrium, the fluoride concentration in the supernatant, C_e, was measured with a fluoride selective electrode connected to an ion meter (PXS-450, Shanghai Kang-Yi Instruments Co., LTD, China) using the method in GB/T 13083-2002 [55]. The equilibrium adsorption capacity of the adsorbent, q_e, was calculated as

$$q_e = \frac{C_0 - C_e}{m/V} \quad (1)$$

where C_0 is the initial fluoride concentration of the solution, C_e is the fluoride concentration after adsorption reached equilibrium, m is the mass of the adsorbent, and V is the solution volume. The curve of q_e vs C_e, i.e., the adsorption isotherm, was then fitted with the Langmuir model and the Freundlich model.

(2) Adsorption kinetics

The adsorption kinetics showed the relationship between the adsorption capacity (q_t) versus the adsorption time (t) from the beginning to the equilibrium of the adsorption process, which reflected the adsorption rate. The adsorption capacity was measured in batch adsorption experiments, as described in our previous work [38]. Here, the adsorbent dosage was 1 g/L, the initial fluoride solution was fixed at 50 mg/L, while the reaction time was variable. The adsorption capacities versus time curves were then fitted with the 1st-order and 2nd-order kinetic models.

(3) Effect of initial solution pH and co-existing anions on the adsorption performance

The effects of the initial solution pH on the adsorption performance were investigated in batch adsorption experiments, as described in our previous work [38]. HCl or NaOH solution was used to adjust the initial pH of the fluoride solution in a range of 2–12. The initial fluoride concentration was set at 50 mg/L. The adsorbent dosage was 1 g/L. The equilibrium adsorption capacities at different initial pH values were measured.

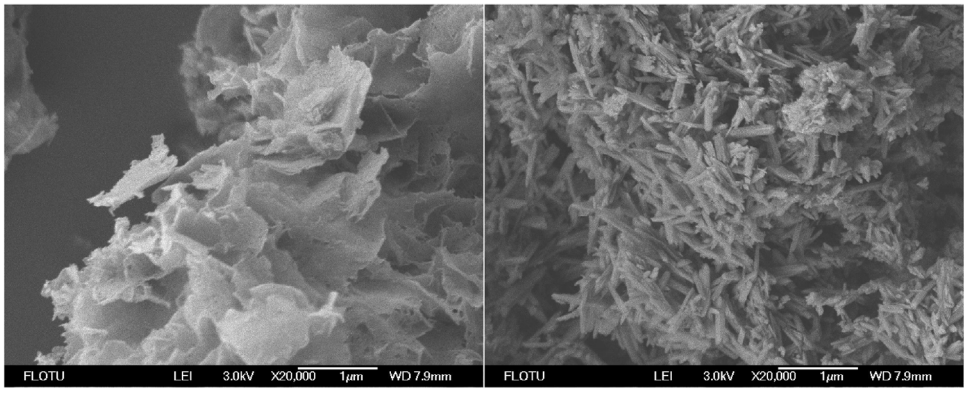

Fig. 1. SEM images of adsorbents (a) with and (b) without ethanol treatment.

As described in our previous work [38], NaCl, $NaNO_3$, Na_2SO_4, Na_2CO_3, and Na_3PO_4 were added into the fluoride solution to play the role of co-existing anions, i.e., Cl^-, NO_3^-, SO_4^{2-}, CO_3^{2-}, and PO_4^{3-}, respectively. The initial pH was adjusted to 7–8 using HCl or NaOH solution. The initial fluoride concentration was set at 4 mg/L. The adsorbent dosage was 1 g/L. The equilibrium adsorption capacities in the presence of different anions were measured.

(4) Regeneration

The regeneration method was described in our previous work [38]. In the adsorption, the initial fluoride concentration was set at 4 mg/L, and the adsorbent dosage was 1 g/L. In the regeneration, NaOH solution was used as regeneration agent. After fluoride adsorption, the used adsorbent was collected and then dispersed in NaOH solution for fluoride desorption. After desorption, the adsorbent was washed with HCl solution for activation, and then used for fluoride adsorption again. The desorption efficiency at different concentrations of NaOH solution and the fluoride adsorption capacity recovery after regeneration were measured. 5 regeneration recycles were conducted.

3. Results and discussion

3.1. Effect of ethanol treatment on adsorbent properties

(1) Structure transformation of the adsorbent

The properties of the adsorbents with and without ethanol treatment were measured and compared. The final precipitation pH was 9.0 and the adsorbent was not heat-treated. The Fe2p and O1 s peaks in the XPS spectra (see Fig. S1) confirm that the adsorbents are iron oxide. The SEM images in Fig. 1 show that the ethanol-treated adsorbent has a flake-like morphology, while the adsorbent without ethanol treatment has a needle-like morphology. The XRD spectra of the adsorbents in Fig. 2 show that the ethanol-treated adsorbent has a totally amorphous structure and the untreated adsorbent has a poorly crystallized goethite structure (α-FeOOH, PDF#29-0713, characteristic peaks: 17.9°, 33.2°, 34.7°, 36.6°, 52.8°, and 59.1°). The SEM and XRD analyses indicate that the ethanol treatment changed the microstructure of the iron oxide adsorbent significantly.

The structural transformation of the adsorbent due to ethanol treatment is illustrated in Fig. 3. During precipitation, the iron oxide nanoprecipitates formed and easily assembled together in the lattice growth pattern of α-FeOOH. Without ethanol treatment, the precipitates were assembled in the drying process, forming a needle-like, crystallized α-FeOOH adsorbent. When treated with ethanol, the nanoprecipitates were dispersed and stabilized by the ethanol molecules adsorbed on their surface. The adsorbed ethanol molecules prevent the assembly of the nanoprecipitates in the drying process, forming a flake-like amorphous adsorbent that was quite different from that without ethanol treatment. Previous reports have indicated the similar structural disturbance of iron oxide/hydroxide in the formation process by adsorbed species like phosphate and nitrate ions through a steric blockage effect [51,56].

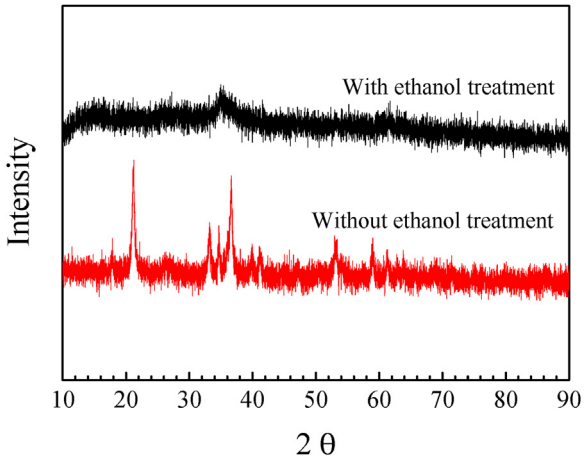

Fig. 2. XRD spectra of the adsorbents with and without ethanol treatment.

To compare the microstructure of the adsorbents, the TEM images of the adsorbents with and without ethanol treatment are shown in Fig. 4. For the ethanol-treated adsorbent, the nanoprecipitate was loosely assembled, forming a flake-like shape, as shown in Fig. 4(a). The adsorbent is porous due to the evaporated ethanol that adsorbed on the nano-precipitate surface, producing a highly specific surface area. In contrast, the adsorbent without ethanol treatment had a dense, crystallized structure, and a low specific surface area, as shown in Fig. 4(b).

To further confirm the effect of the ethanol treatment, the ethanol-treated precipitate was re-washed using deionized water to remove the ethanol before drying, and the microstructure of the re-washed adsorbent was examined and compared to that of the adsorbents with and without ethanol treatment. The re-washed adsorbent had a needle-like morphology and a crystal spectrum corresponding to that of goethite (α-FeOOH, PDF#29-0713) just as the adsorbent without ethanol treatment, as shown in the SEM images in Fig. S2 and the XRD spectrum in Fig. S3, thus confirming that the microstructural change of the adsorbent was due to

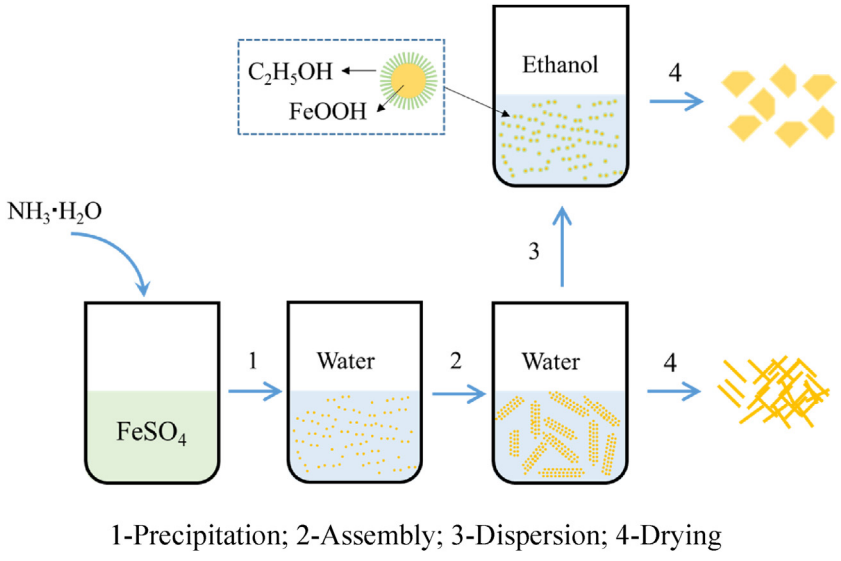

Fig. 3. Structural transformation of the adsorbent during ethanol treatment.

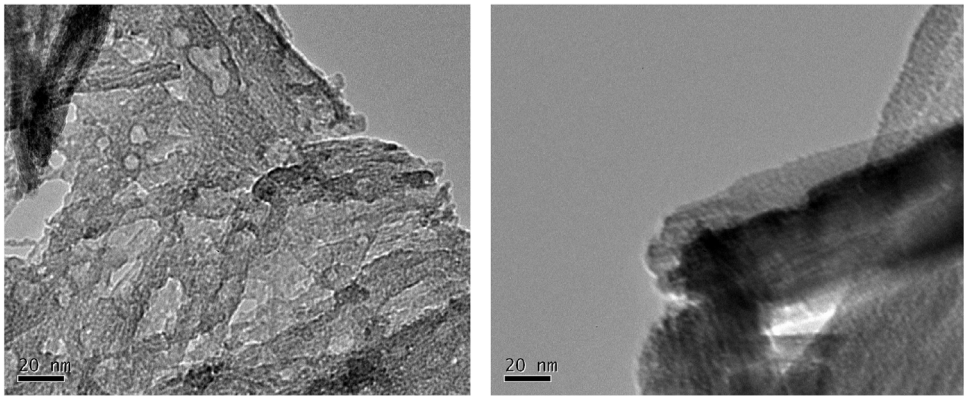

Fig. 4. TEM images of adsorbents (a) with and (b) without ethanol treatment.

Table 1
Adsorption capacities and specific surface area of the adsorbents with and without ethanol treatment.

Ethanol treatment	With	Without
Q_e([F]$_0$=50 mg/L), mg/g	24.6	9.2
Q_e([F]$_0$=500 mg/L), mg/g	62.3	10.9
SSA, m^2/g	150.4	12.6

the effects of ethanol treatment. The appearance of the crystallized structure in the re-washed precipitate indicated that the ethanol molecules were weakly adsorbed to the surface of the precipitates and easily removed.

(2) Specific surface area and adsorption capacity

The specific surface areas of the adsorbents with and without ethanol treatment were determined by N_2 adsorption analysis. As shown in Table 1, the specific surface areas of the adsorbent with and without ethanol treatment were 12.6 m^2/g and 150.4 m^2/g, respectively. This indicates that the ethanol-treated adsorbent had more surface active sites for adsorption. The N_2 adsorption-desorption isotherms and the corresponding pore size distribution curves (analyzed by DFT method) of the adsorbents are shown in Fig. S4.

The adsorption capacities of the adsorbents with and without ethanol treatment were determined and compared (Table 1). The adsorption capacity of the ethanol-treated adsorbent with an initial fluoride concentration of 50 mg/L was 24.6 mg/g, much higher than 9.2 mg/g for the adsorbent without ethanol treatment. When the initial fluoride concentration increased to 500 mg/L, the ethanol-treated adsorbent reached a higher equilibrium adsorption capacity of 62.3 mg/g, almost five times higher than the capacity of the adsorbent without ethanol treatment. The increase of the adsorption capacity difference is mainly attributed to the increase in the number of surface active sites for fluoride removal, indicating that the facile ethanol-treatment significantly increases the adsorption capacity of the iron oxide adsorbent.

3.2. *Effects of preparation conditions on adsorbent properties*

(1) Effects of final precipitation pH

In order to optimize the adsorbent preparation, the effects of the final precipitation pH on the adsorption capacity for the adsorbents with and without ethanol treatment were investigated. The set final pH values were 7.6, 8.0, 9.0, and 9.6, which correspond to 9 mL, 18 mL, 29 mL, and 40 mL of titrated ammonia, respectively.

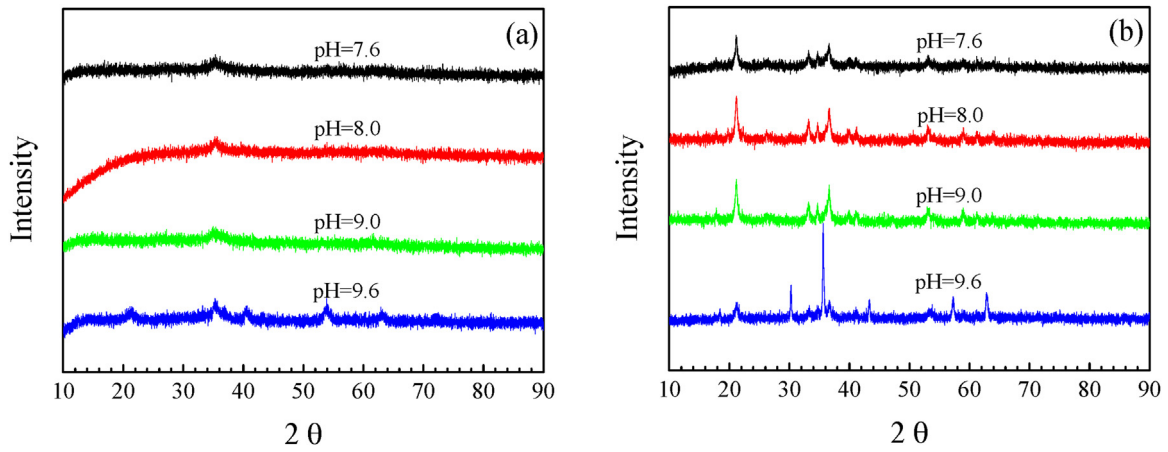

Fig. 5. XRD spectra of the adsorbents (a) with and (b) without ethanol treatment at different final precipitation pH.

Table 2
Equilibrium adsorption capacity and specific surface area of the adsorbents with and without ethanol treatment at different final precipitation pH ($[F^-]_0$ = 50 mg/L).

Ammonia titration, mL	Final precipitation pH	With ethanol treatment		Without ethanol treatment	
		Q_e, mg/g	SSA, m^2/g	Q_e, mg/g	SSA, m^2/g
9	7.6	24.4	128.0	11.6	8.8
18	8.0	24.1	123.7	8.4	11.4
29	9.0	24.6	150.4	9.2	12.9
40	9.6	12.7	50.3	10.5	19.8

SEM images and XRD spectra of the adsorbents were taken. The morphology of the adsorbents with the final precipitation pH values of 7.6 and 8.0 before and after ethanol treatment was very similar to that with a final precipitation pH of 9.0, as shown in Fig. 1. The XRD spectra patterns shown in Fig. 5 indicate that the adsorbents with and without ethanol treatment did not change when the final precipitation pH was ≤9.0. The morphologies of the adsorbents prepared with a final precipitation pH of 9.6 are shown in Fig. S5, and the XRD spectra of the adsorbents are shown in Fig. 5. When the final precipitation pH was 9.6, the precipitate without ethanol treatment was a mixture of sphere-like particles and tiny rods with a crystal spectrum corresponding to that of maghemite (γ-Fe_2O_3, PDF#39-1346, characteristic peaks: 30.3°, 35.6°, 43.3°, 53.8°, 57.3°, 62.9°). The small peak at 21.2° was assigned to α-FeOOH, indicating that the adsorbent contained a small portion of α-FeOOH. As in the case with a lower final precipitation pH, the ethanol-treated adsorbent had a flake-like morphology and the α-FeOOH crystal structure was inhibited. However, the ethanol-treated adsorbent had a rougher surface and more crystalline constituents than the precipitate prepared at a lower pH, in accordance with the needle-like and sphere-like portions in the SEM image and the broad peaks in the XRD spectra. It is inferred that the nano-γ-Fe_2O_3 precipitate formed at pH 9.6 was more difficult to be dispersed than the α-FeOOH precipitate; therefore, the ethanol treatment was less effective in preventing the crystallization. The ethanol treatment effects are different for different types of the formed iron oxide, i.e., different final precipitation pH.

The equilibrium adsorption capacity at the initial fluoride concentration $[F]_0$ = 50 mg/L and the specific surface area of the adsorbents with and without ethanol treatment with a different final precipitation pH are shown in Table 2. The N_2 adsorption-desorption isotherms and the corresponding pore size distribution curves (analyzed by DFT method) of the adsorbents are shown in Fig. S4. It is indicated that the ethanol treatment can increase the adsorption capacity and the specific surface area at the final precipitation pH below 9.0, but the increase at pH 9.6 was less significant. When the final precipitation pH was less than 9.6, the precipitate was α-FeOOH, the specific surface area of the ethanol-treated adsorbent was 120–150 m^2/g, and the adsorption capacity was 24–25 mg/g. When the final precipitation pH reached 9.6, the precipitate was γ-Fe_2O_3, the specific surface area of the ethanol-treated adsorbent was only 50.3 m^2/g, and the adsorption capacity of the ethanol-treated adsorbent was only 12.7 mg/g. The ethanol treatment causes less effective structure transformation of the precipitate with a final precipitation pH of 9.6.

Therefore, the increase in the final precipitation pH caused the crystal phase transformation of the iron oxide precipitate, which affects the effects of the ethanol treatment, leading to different adsorption performance of the ethanol-treated adsorbent. To obtain a high adsorption capacity of the ethanol-treated adsorbent, the final precipitation pH should not exceed 9.0, i.e., the iron oxide precipitate should have a goethite structure.

(2) Effects of thermal treatment

The effects of thermal treatment on the adsorbent properties were investigated at different temperatures on the ethanol-treated adsorbent with the final precipitation pH of 9.0. The SEM images in Fig. S6 show that the aggregation in the heat-treated adsorbents was enhanced with the temperature increase, and some fine needle-like and sphere-like parts appeared. The XRD spectra in Fig. 6 confirmed the increase of in the amount of the crystallized constituent in the heat-treated adsorbent. After thermal treatment at 100 °C and 200 °C, the adsorbent was poorly crystallized maghemite (γ-Fe_2O_3, PDF#39-1346). After thermal treatment at 300 °C or higher, the adsorbent was hematite (α-Fe_2O_3, PDF#33-0664).

The adsorption capacity and specific surface area of the heat-treated adsorbents at different temperature are shown in Table 3. The N_2 adsorption-desorption isotherms and the corresponding pore size distribution curves (analyzed by DFT method) of the adsorbents are shown in Fig. S7. Basically, the adsorption capacity and the specific surface area decreased significantly with the

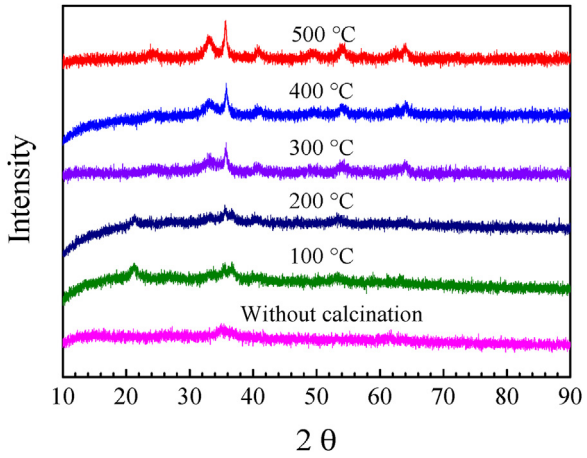

Fig. 6. XRD spectra of the ethanol-treated adsorbents with thermal treatment at different temperatures.

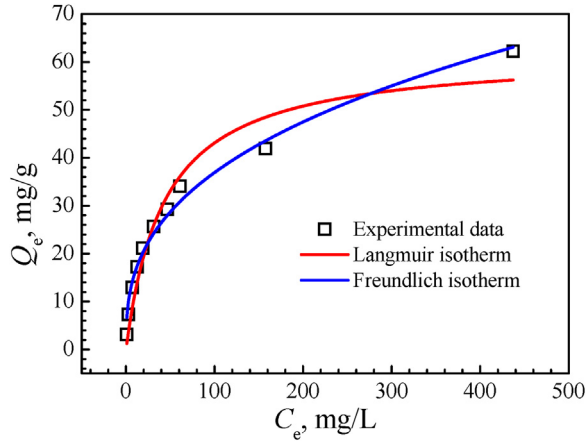

Fig. 7. Adsorption isotherms of the ethanol-treated adsorbent (adsorbent dosage = 1 g/L).

Table 3
Equilibrium adsorption capacity ($[F^-]_0$ = 50 mg/g) and specific surface area of the heat-treated adsorbents at different temperatures.

T, ° C	No	100	200	300	400	500
Adsorption capacity, mg/g	24.6	19.0	17.0	13.3	11.5	9.5
SSA, m^2/g	150.4	94.7	72.1	51.3	28.2	32.8

increase in the thermal treatment temperature, corresponding to the increase in the crystallization degree.

Therefore, to obtain high adsorption performance, the adsorbent should not be thermally treated to avoid the enhancement of crystallization. The ethanol-treated adsorbent with a final precipitation pH of 9.0 and with no thermal treatment was used for further investigations.

3.3. Adsorption performances of the ethanol-treated adsorbent

(1) Adsorption isotherm

The adsorption isotherm of the adsorbent is measured and shown in Fig. 7. The experimental data were fitted using the Langmuir model and Freundlich model [57]:

$$Q_e = \frac{Q_{L,max} b C_e}{1 + bC_e} \quad \text{(Langmuir model)} \tag{2}$$

(3) $Q_e = K_f C_e^{1/n}$ (Freundlich model)where $Q_{L,max}$, b, K_f, and n are the fitting parameters of the models, reflecting the adsorption ability of the adsorbent.

The fitting results are shown in Table 4. Both the Langmuir model and the Freundlich model had a high correlation coefficient with the adsorption isotherm. The Langmuir model fitted better with the adsorption isotherm when the equilibrium fluoride concentration was lower than 100 mg/L, indicating the occurrence of monolayer adsorption. When the equilibrium fluoride concentration was higher than 100 mg/L, the Freundlich model fitted better with the adsorption isotherm, indicating a heterogeneous multilayer adsorption of the adsorbent surface for fluoride [57]. Since the adsorption capacity of an adsorbent is usually given by the Langmuir maximum adsorption capacity in literature, the Langmuir maximum adsorption capacity of the adsorbent was used for comparison with other fluoride removal adsorbents. The Langmuir maximum adsorption capacity reached a high value of 60.8 mg/g. Compared with other iron-based adsorbents, the iron-oxide adsorbent used in this work had a relatively high adsorption capacity, as is shown in Table 5. Since no expensive or harmful additive (like Ti, Cr, and graphene oxide) was needed in the adsorbent synthesis, it had a high cost efficiency.

Table 5
Langmuir maximum adsorption capacity of this work compared with those of other iron-based adsorbents in literature.

Adsorbents	Langmuir $Q_{L,max}$, mg/g	Ref.
β-FeOOH@GO	7.1	[20]
γ-Fe_2O_3	7.9	[21]
β-FeOOH	7.0	[34]
$FeCO_3$	1.7	[35]
Fe-Ti oxide	47.3	[39]
Fe-Zr oxide	8.2	[41]
Fe-Al oxide	17.7	[42]
Fe-Sn oxide	10.5	[43]
Fe-Cr oxide	16.3	[44]
Amorphous Fe oxide	60.8	This work

(2) Adsorption kinetics

The adsorption kinetic curve of the adsorbent is shown in Fig. 8. The adsorption kinetic data were fitted using the 1st- and 2nd-order kinetic models [47]:

$$\frac{dq}{dt} = k_1 (q_e - q) \tag{4}$$

$$\frac{dq}{dt} = k_2 (q_e - q)^2 \tag{5}$$

The integral expressions are:

$$q = q_e (1 - e^{-k_1 t}) \tag{6}$$

$$q = k_2 q_e^2 t / (1 + k_2 q_e t) \tag{7}$$

Table 4
Fitting parameters of the adsorption isotherms (adsorbent dosage = 1 g/L).

Fitted model	Langmuir			Freundlich		
Parameter	$Q_{L,max}$, mg/g	b, L/mg	R^2	K_f, mg/g	n	R^2
Value	60.8	0.06	0.9898	5.24	2.18	0.9907

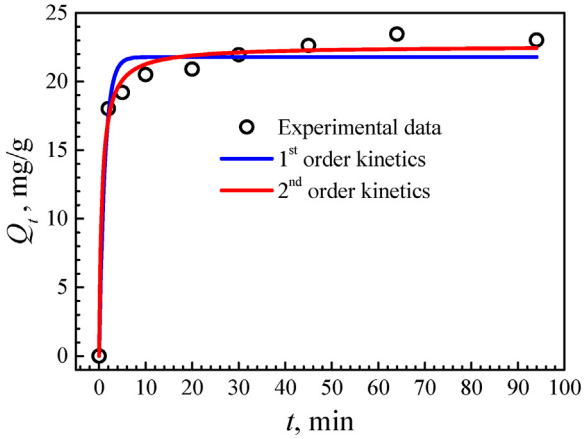

Fig. 8. Adsorption kinetics of the ethanol-treated adsorbent ($[F^-]_0$ = 50 mg/L, adsorbent dosage = 1 g/L).

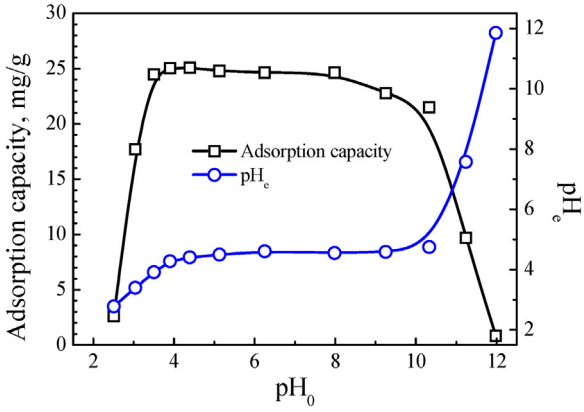

Fig. 9. Effects of the initial solution pH on the equilibrium adsorption capacity ($[F^-]_0$ = 50 mg/L).

where k_1 and k_2 are the rate constants of the 1st- and 2nd-order kinetic models, respectively; q_e is the equilibrium adsorption capacity; and q is the adsorption capacity at time t.

Fig. 8 shows that the adsorption was very fast and 80% of the equilibrium adsorption capacity was achieved within 2 min. The 1st- and 2nd-order kinetic models were used to fit the adsorption kinetic data, and the fitting parameters are shown in Table 6. According to the correlation coefficient, the 2nd-order kinetic model fitted better with the experimental data.

(3) Effects of the initial solution pH

The effects of the initial solution pH on the adsorption performance of the adsorbent were investigated and shown in Fig. 9. In the pH range of 3.5–10.3, the equilibrium adsorption capacities of the adsorbent have almost no change, indicating that the adsorbent had a wide pH range suitable for fluoride adsorption. When the pH was <3.5, the formation of the weak acid HF increased. The adsorbent surface had a weak attraction to HF in the solution, resulting in a decreased adsorption capacity. When the pH was >10.3, the abundant OH^- competed with the F^- ions for the active sites of the adsorbent surface, leading to the decrease in the adsorption capacity [23,38,58]. The equilibrium solution pH is also shown in Fig. 9. A pH buffering effect of the iron oxide was observed [38]. When the initial pH was lower than 10.3, the equilibrium pH was lower than the pH_{ZPC} of the adsorbent (pH_{ZPC}=5.4, see Fig. S8), the adsorbent carried positive surface charge and preferred to adsorb fluoride ions. When the initial pH was higher than 10.3, the equilibrium pH was higher than 5.4, the adsorbent had negative surface charge, which cause the adsorption capacity decrease.

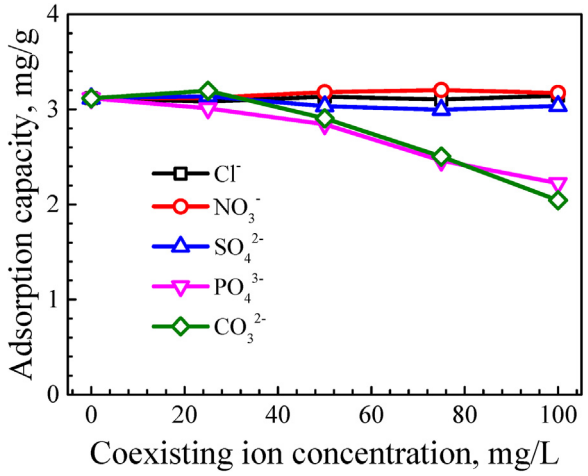

Fig. 10. Effects of coexisting ions on the adsorption capacity ($[F^-]_0$ = 4 mg/L; initial pH 7–8).

(4) Effects of co-existing ions in adsorption

The equilibrium fluoride adsorption capacity of the adsorbent in the presence of some common anions was studied, as is shown in Fig. 10. Cl^-, NO_3^- and SO_4^{2-} had almost no effect on the fluoride adsorption capacity even when the co-existing anion concentration was 25 times that of the fluoride concentration, indicating the high fluoride affinity of the adsorbent even in high salinity water [59]. CO_3^{2-} and PO_4^{3-} at a high concentration did reduce the fluoride adsorption capacity, but their effect was negligible until the co-existing anion concentration was 10 times higher than the fluoride concentration. In fact, the concentration of PO_4^{3-} in groundwater is usually less than 5 mg/L [60], which has no effect on fluoride removal. At a typical concentration of about 100 mg/L for CO_3^{2-} in groundwater [59], a high fluoride removal efficiency is still obtained with the adsorbent, indicating a higher selectivity for fluoride than that of other adsorbents reported in literature [60–63].

(5) Fluoride desorption

The fluoride desorption efficiencies of the adsorbent using NaOH solution of 0.001 M, 0.01 M and 0.1 M were 19.9%, 85.3% and 95.6%, respectively, indicating that the used adsorbent can be regenerated by using NaOH solution. The fluoride adsorption capacity recovery of the adsorbent after regeneration with 0.1 M NaOH solution is shown in Table 7. It indicates that the adsorbent had a high regeneration efficiency. After 5 recycles, over 85% of the initial adsorption

Table 6
Fitting parameters of the adsorption kinetics ($[F^-]_0$ = 50 mg/L, adsorbent dosage = 1 g/L).

	1st kinetics			2nd kinetics		
Parameter	Q_e, mg/g	k_1, min^{-1}	R^2	Q_e, mg/g	k_2, g mg^{-1} min^{-1}	R^2
Value	21.55	0.85	0.9689	22.58	0.07	0.9874

Table 7
The fluoride adsorption capacity recovery of the adsorbent after each regeneration recycle ($[F^-]_0$=4 mg/L, desorption time 10 min). 0: initial adsorption capacity, 100%.

Recycles	0	1	2	3	4	5
F^- adsorption recovery, %	100	93.9	92.8	92.6	90.0	85.8

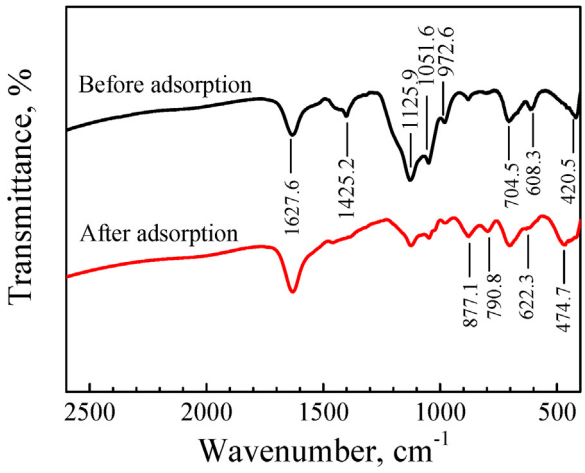

Fig. 11. FT-IR spectra of the ethanol-treated adsorbent before and after fluoride adsorption ($[F^-]_0$ = 500 mg/L).

capacity was recovered, indicating a high reusability of the adsorbent for a long term.

3.4. Adsorption mechanism

The FT-IR spectra of the adsorbent before and after adsorption are shown in Fig. 11. The peak at 1627.6 cm^{-1} was assigned to the bending vibration of water [38]. The peak at 1425.2 cm^{-1} was assigned to the bending vibration of C—H bond in the residual ethanol [64], which was removed from the adsorbent after soaking in water. It was confirmed that the adsorbent after soaking in deionized water had the same adsorption capacity and the residue ethanol had no contribution to the adsorption of fluoride. The broad band from 1272.2 cm^{-1} to 941.3 cm^{-1} consisted of three peaks at 1125.9 cm^{-1}, 1051.6 cm^{-1}, and 972.6 cm^{-1}, representing the bending vibration of the metal hydroxyl groups [20,39]. The peaks at 877.1 cm^{-1} and 790.8 cm^{-1} were attributed to the hydrogen bond [58,65]. For bands in the range of 700–400 cm^{-1}, the peaks at 704.5 cm^{-1}, 608.3 cm^{-1}, and 420.5 cm^{-1} for the adsorbent before adsorption, and at 704.5 cm^{-1}, 622.3 cm^{-1}, and 474.7 cm^{-1} for the adsorbent after adsorption, were assigned to the Fe-O bond in the FeOOH oxide [66].

Table 8
Changes of the XPS O1 s peak of the adsorbent before and after fluoride adsorption ($[F^-]_0$ = 500 mg/L).

Sample	Peak	Binding energy, eV	FWHM, eV	Mole content, %
Before adsorption	O^{2-}	530.06	1.24	23.5
	OH^-	531.65	1.66	76.5
After adsorption	O^{2-}	529.86	1.16	34.2
	OH^-	531.31	1.69	66.4

After adsorption, the band from 1272.2 cm^{-1} to 941.3 cm^{-1} weakened significantly, indicating that the hydroxyl groups on the adsorbent surface played a role in the adsorption. The peaks at 880.4 cm^{-1} and 786.3 cm^{-1} strengthened, indicating that the hydrogen bond was strengthened, which was inferred to be due to the adsorbed fluoride having a higher electronegativity than oxygen in the formation of a hydrogen bond. The location shift of the Fe-O bands from 608.3 cm^{-1} to 622.3 cm^{-1} and from 420.5 cm^{-1} to 474.7 cm^{-1} indicated the formation of a new bond between Fe and fluoride.

For further clarification of the adsorption mechanism, the XPS spectra before and after adsorption are shown in Fig. S9. After adsorption, a new peak assigned to F1 s occurred at 684.5 eV, confirming the fluoride adsorption on the adsorbent surface. The mole ratio of F on the surface of the adsorbent increased to 18.1% and the mole ratio of O decreased by 16.2% after adsorption, as is shown in Table S1, indicating that ion exchange between fluoride and some oxygen-containing groups on the adsorbent surface occurred during the adsorption process. The O1 s XPS spectra before and after adsorption were deconvoluted into two peaks, which were assigned to hydroxyl (OH) group and oxygen anion (O^{2-}), respectively, as is shown in Fig. 12. The binding energy and relative content of the OH and O^{2-} groups are shown in Table 8. The content of the OH group decreased significantly after adsorption, indicating that it was the OH groups that were replaced by the fluoride ions. The decrease of binding energy for OH and O^{2-} groups are inferred to be caused by the electron-donating conjugated effect of fluoride which increased the electron cloud density and the electron shielding effect of the O atoms.

Therefore, the adsorption mechanism of the iron oxide adsorbent is expressed as:

$$Fe-OH + F^- \rightarrow Fe-F + OH^- \quad (8)$$

According to Eq. (8), higher fluoride concentration caused more OH^- release [38]. The final pH of fluoride solution after adsorp-

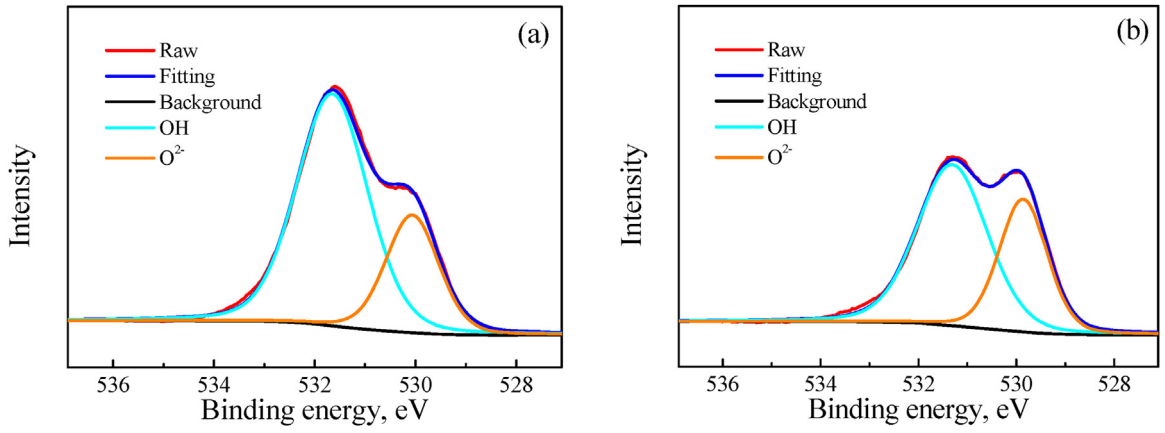

Fig. 12. XPS spectra of O1 s peak for the ethanol-treated adsorbent (a) before and (b) after fluoride adsorption.

Table 9
The initial pH of the fluoride solution and the final pH after adsorption for different initial fluoride concentration.

$[F^-]_0$, mg/L	0	50	100	200	500
pH_0	7.0	7.1	7.2	7.3	7.4
pH_e	3.8	4.6	4.9	5.3	5.8

tion for different initial fluoride concentration is shown in Table 9. The fluoride solution was prepared by dissolving NaF in deionized water, without pH adjustment. Since HF is a weak acid, the solution pH increases as the fluoride concentration increase, but generally in the range of 7.0-8.0. The buffering effect of the adsorbent and the exchange of fluoride and OH^- also affect the final pH of the solution. The buffering effect is the same for all the solutions, causing the final pH decrease, as shown in Fig. 9. The exchange of fluoride and OH^- is enhanced as the fluoride concentration increases, causing the increase of the final pH. Table 9 shows that the final pH of the solution increased from 3.8 to 5.8 when the initial fluoride concentration increased from 0 to 500 mg/L. The larger increase of the final pH confirmed that the ion exchange occurred between fluoride and the hydroxyl groups and higher fluoride concentration caused more OH^- release.

4. Conclusions

A cost-effective iron-oxide adsorbent with a high adsorption capacity for fluoride was prepared by a facile wet-chemical precipitation method and ethanol treatment. The Langmuir maximum adsorption capacity reached a high value of 60.8 mg/g. The ethanol-treated adsorbent had a high adsorption rate, and 80% of the equilibrium adsorption capacity was achieved within 2 min. The adsorbent had a high fluoride adsorption capacity in a wide pH range of 3.5–10.3 and a high selectivity for fluoride in the presence of common anions. The obtained adsorbent was highly cost-effective for fluoride removal from drinking water.

The ethanol treatment caused the microstructure transformation of the adsorbent from a poorly crystallized needle-like goethite precipitate to a totally amorphous adsorbent with a flake-like morphology, which significantly increased the specific surface area of the adsorbent, increasing the adsorption capacity for fluoride. To obtain a high specific surface area and adsorption capacity after ethanol treatment, the final precipitation pH should be below 9.0 to produce a poorly crystallized α-FeOOH structured precipitate. The adsorption mechanism was determined to be due to ion exchange between fluoride and the hydroxyl groups on the adsorbent surface.

Acknowledgment

This work is supported by the National High Technology Research and Development Program (863 Program, No. 2012AA062605) and the National Natural Science Foundation of China (NSFC No. 21176134).

Appendix A. Supplementary data

Supplementary data associated with this article can be found, in the online version, at http://dx.doi.org/10.1016/j.apsusc.2017.06.159.

References

[1] A. Bhatnagar, E. Kumar, M. Sillanpää, Fluoride removal from water by adsorption–A review, Chem. Eng. J. 171 (2011) 811–840.
[2] GB 5749-2006, Standards for drinking water quality, CN-GB.
[3] Meenakshi, R.C. Maheshwari, Fluoride in drinking water and its removal, J. Hazard, Mater. 137 (2006) 456–463.
[4] M. Mohapatra, S. Anand, B. Mishra, D. Giles, P. Singh, Review of fluoride removal from drinking water, J. Environ. Manage. 91 (2009) 67–77.
[5] M. Habuda-Stanić, M. Ravančić, A. Flanagan, A Review on Adsorption of Fluoride from Aqueous Solution, Materials 7 (2014) 6317–6366.
[6] H. Cai, L. Xu, G. Chen, C. Peng, F. Ke, Z. Liu, D. Li, Z. Zhang, X. Wan, Removal of fluoride from drinking water using modified ultrafine tea powder processed using a ball-mill, Appl. Surf. Sci. 375 (2016) 74–84.
[7] H.M. Cai, G.J. Chen, C.Y. Peng, Z.Z. Zhang, Y.Y. Dong, G.Z. Shang, X.H. Zhu, H.J. Gao, X.C. Wan, Removal of fluoride from drinking water using tea waste loaded with Al/Fe oxides: a novel, safe and efficient biosorbent, Appl. Surf. Sci. 328 (2015) 34–44.
[8] S. Saha, Treatment of aqueous effluent for fluoride removal, Water Res. 27 (1993) 1347–1350.
[9] E.J. Reardon, Y.X. Wang, A limestone reactor for fluoride removal from wastewaters, Environ. Sci. Technol. 34 (2000) 3247–3253.
[10] L.D. Guo, B.J. Hunt, P.H. Santschi, Ultrafiltration behavior of major ions (Na, Ca, Mg, F, Cl, and SO_4) in natural waters, Water Res. 35 (2001) 1500–1508.
[11] A. Lhassani, M. Rumeau, D. Benjelloun, M. Pontie, Selective demineralization of water by nanofiltration application to the defluorination of brackish water, Water Res. 35 (2001) 3260–3264.
[12] P. Sehn, Fluoride removal with extra low energy reverse osmosis membranes: three years of large scale field experience in Finland, Desalination 223 (2008) 73–84.
[13] M. Tahaikt, I. Achary, M.A.M. Sahli, Z. Amor, M. Taky, A. Alami, A. Boughriba, M. Hafsi, A. Elmidaoui, Defluoridation of Moroccan groundwater by electrodialysis: continuous operation, Desalination 189 (2006) 215–220.
[14] F. Shen, X. Chen, P. Gao, G. Chen, Electrochemical removal of fluoride ions from industrial wastewater, Chem. Eng. Sci. 58 (2003) 987–993.
[15] K. Sasaki, N. Fukumoto, S. Moriyama, Q. Yu, T. Hirajima, Chemical regeneration of magnesium oxide used as a sorbent for fluoride, Sep. Purif. Technol. 98 (2012) 24–30.
[16] Y. Chen, Q. Zhang, L. Chen, H. Bai, L. Li, Basic aluminum sulfate@graphene hydrogel composites: preparation and application for removal of fluoride, J. Mater. Chem. A 1 (2013) 13101.
[17] A.L. Srivastav, P.K. Singh, V. Srivastava, Y.C. Sharma, Application of a new adsorbent for fluoride removal from aqueous solutions, J. Hazard. Mater. 263 (Pt 2) (2013) 342–352.
[18] T.G. Li, D.L. Xie, C.H. He, X.J. Xu, B. Huang, R. Nie, S.L. Liu, Z.Y. Duan, W. Liu, Simultaneous adsorption of fluoride and hexavalent chromium by synthetic mesoporous alumina: performance and interaction mechanism, RSC Adv. 6 (2016) 48610–48619.
[19] E. Kumar, A. Bhatnagar, W. Hogland, M. Marques, M. Sillanpää, Interaction of anionic pollutants with Al-based adsorbents in aqueous media–A review, Chem. Eng. J. 241 (2014) 443–456.
[20] Y.Y. liu, J.X. Lv, W. Jin, Y.P. Zhao, Defluoridation by rice spike-like akaganeite anchored graphene oxide, RSC Adv. 6 (2016) 11240–11249.
[21] S. Asuha, Y.M. Zhao, S. Zhao, W. Deligeer, Synthesis of mesoporous maghemite with high surface area and its adsorptive properties, Solid State Sci. 14 (2012) 833–839.
[22] Q. Zhou, X. Lin, B. Li, X. Luo, Fluoride adsorption from aqueous solution by aluminum alginate particles prepared via electrostatic spinning device, Chem. Eng. J. 256 (2014) 306–315.
[23] K. Zhang, S. Wu, X. Wang, J. He, B. Sun, Y. Jia, T. Luo, F. Meng, Z. Jin, D. Lin, W. Shen, L. Kong, J. Liu, Wide pH range for fluoride removal from water by MHS-MgO/$MgCO_3$ adsorbent: kinetic, thermodynamic and mechanism studies, J. Coll. Interf. Sci. 446 (2015) 194–202.
[24] Z. Jin, Y. Jia, T. Luo, L.T. Kong, B. Sun, W. Shen, F.L. Meng, J.H. Liu, Efficient removal of fluoride by hierarchical MgO microspheres: performance and mechanism study, Appl. Surf. Sci. 357 (2015) 1080–1088.
[25] J. Liu, W.Y. Li, Y.G. Liu, Q.H. Zeng, S. Hong, Titanium(IV) hydrate based on chitosan template for defluoridation from aqueous solution, Appl. Surf. Sci. 293 (2014) 46–54.
[26] L.H. Velazquez-Jimenez, R.H. Hurt, J. Matos, J.R. Rangel-Mendez, Zirconium-carbon hybrid sorbent for removal of fluoride from water: oxalic acid mediated Zr(IV) assembly and adsorption mechanism, Environ. Sci. Technol. 48 (2014) 1166–1174.
[27] J. He, T.S. Siah, J. Paul Chen, Performance of an optimized Zr-based nanoparticle-embedded PSF blend hollow fiber membrane in treatment of fluoride contaminated water, Water Res. 56 (2014) 88–97.
[28] J. Zhu, X. Lin, P. Wu, Q. Zhou, X. Luo, Fluoride removal from aqueous solution by Al(III)-Zr(IV) binary oxide adsorbent, Appl. Surf. Sci. 357 (2015) 91–100.
[29] D.W. Cho, B.H. Jeon, Y. Jeong, I.H. Nam, U.K. Choi, R. Kumar, H. Song, Synthesis of hydrous zirconium oxide-impregnated chitosan beads and their application for removal of fluoride and lead, Appl. Surf. Sci. 372 (2016) 13–19.
[30] L. Chen, T.-J. Wang, H.-X. Wu, Y. Jin, Y. Zhang, X.-M. Dou, Optimization of a Fe-Al-Ce nano-adsorbent granulation process that used spray coating in a fluidized bed for fluoride removal from drinking water, Powder Technol. 206 (2011) 291–296.
[31] D.D. Tang, G.K. Zhang, Efficient removal of fluoride by hierarchical Ce-Fe bimetal oxides adsorbent: thermodynamics, kinetics and mechanism, Chem. Eng. J. 283 (2016) 721–729.
[32] S. Zhang, Y. Lu, X. Lin, X. Su, Y. Zhang, Removal of fluoride from groundwater by adsorption onto La(III)- Al(III) loaded scoria adsorbent, Appl. Surf. Sci. 303 (2014) 1–5.

[33] S.X. Wen, Y.L. Wang, S.X. Dong, Performance and characteristics of fluoride adsorption using nanomagnetite graphite-La adsorbent, RSC Adv. 5 (2015) 89594–89602.
[34] Y. Zhang, X. Lin, Q. Zhou, X. Luo, Fluoride adsorption from aqueous solution by magnetic core-shell Fe_3O_4@alginate-La particles fabricated via electro-coextrusion, Appl. Surf. Sci. 389 (2016) 34–45.
[35] E. Kumar, A. Bhatnagar, M. Ji, W. Jung, S.-H. Lee, S.-J. Kim, G. Lee, H. Song, J.-Y. Choi, J.-S. Yang, B.-H. Jeon, Defluoridation from aqueous solutions by granular ferric hydroxide (GFH), Water Res. 43 (2009) 490–498.
[36] Q. Liu, H. Guo, Y. Shan, Adsorption of fluoride on synthetic siderite from aqueous solution, J. Fluorine Chem. 131 (2010) 635–641.
[37] D. Mohan, C.U. Pittman Jr., Arsenic removal from water/wastewater using adsorbents-A critical review, J. Hazard. Mater. 142 (2007) 1–53.
[38] C. Zhang, Y. Li, T.-J. Wang, Y. Jiang, H. Wang, Adsorption of drinking water fluoride on a micron-sized magnetic Fe_3O_4@Fe-Ti composite adsorbent, Appl. Surf. Sci. 363 (2016) 507–515.
[39] L. Chen, B. He, S. He, T. Wang, C. Su, Y. Jin, Fe-Ti oxide nano-adsorbent synthesized by co-precipitation for fluoride removal from drinking water and its adsorption mechanism, Powder Technol. 227 (2012) 3–8.
[40] V. Lenoble, C. Laclautre, V. Deluchat, B. Serpaud, J.C. Bollinger, Arsenic removal by adsorption on iron(III) phosphate, J. Hazard. Mater. 123 (2005) 262–268.
[41] K. Biswas, D. Bandhoyapadhyay, U. Ghosh, Adsorption kinetics of fluoride on iron(III)-zirconium(IV) hybrid oxide, Adsorption 13 (2007) 83–94.
[42] K. Biswas, S.K. Saha, U.C. Ghosh, Adsorption of fluoride from aqueous solution by a synthetic iron(III)-aluminum(III) mixed oxide, Ind. Eng. Chem. Res. 46 (2007) 5346–5356.
[43] K. Biswas, K. Gupta, U. Ghosh, Adsorption of fluoride by hydrous iron(III)-tin(IV) bimetal mixed oxide from the aqueous solutions, Chem. Eng. J. 149 (2009) 196–206.
[44] K. Biswas, S. Debnath, U. Ghosh, Physicochemical aspects on fluoride adsorption for removal from water by synthetic hydrous iron(III)-chromium(III) mixed oxide, Sep. Sci. Technol. 45 (2010) 472–485.
[45] X.M. Wu, Y. Zhang, X.M. Dou, B. Zhao, M. Yang, Fluoride adsorption on an Fe-Al-Ce trimetal hydrous oxide: characterization of adsorption sites and adsorbed fluorine complex species, Chem. Eng. J. 223 (2013) 364–370.
[46] C. Zhang, L. Chen, T.-J. Wang, C.-L. Su, Y. Jin, Synthesis and properties of a magnetic core-shell composite nano-adsorbent for fluoride removal from drinking water, Appl. Surf. Sci. 317 (2014) 552–559.
[47] L. Chen, S. He, B.-Y. He, T.-J. Wang, C.-L. Su, C. Zhang, Y. Jin, Synthesis of iron-doped titanium oxide nanoadsorbent and its adsorption characteristics for fluoride in drinking water, Ind. Eng. Chem. Res. 51 (2012) 13150–13156.
[48] P. Oulego, M.A. Villa-Garcia, A. Laca, M. Diaz, The effect of the synthetic route on the structural textural, morphological and catalytic properties of iron(III) oxides and oxyhydroxides, Dalton Trans. 45 (2016) 9446–9459.
[49] H.X. Xiong, L.X. Zhou, Synthesis of iron oxyhydroxides of different crystal forms and their roles in adsorption and removal of Cr(VI) from aqueous solutions, Acta Petrologica Et Mineralogica 27 (2008) 559–566.
[50] P. Refait, M. Reffass, J. Landoulsi, R. Sabot, M. Jeannin, Role of phosphate species during the formation and transformation of the Fe(II-III) hydroxycarbonate green rust, Colloids Surf. A: Physicochem. Eng. Asp. 299 (2007) 29–37.
[51] P. Refait, M. Reffass, J. Landoulsi, R. Sabot, M. Jeannin, Role of nitrite species during the formation and transformation of the Fe(II-III) hydroxycarbonate green rust, Colloids Surf. A: Physicochem. Eng. Asp. 459 (2014) 225–232.
[52] T. Ishikawa, S. Miyamoto, K. Kandori, T. Nakayama, Influence of anions on the formation of (-FeOOH rusts, Corros. Sci. 47 (2005) 2510–2520.
[53] W.J. Chen, P.J. Tsai, Y.C. Chen, Functional Fe_3O_4/TiO_2 core/shell magnetic nanoparticles as photokilling agents for pathogenic bacteria, Small 4 (2008) 485–491.
[54] T. Ishikawa, R. Katoh, A. Yasukawa, K. Kandori, T. Nakayama, F. Yuse, Influences of metal ions on the formation of (-FeOOH particles, Corros. Sci. 43 (2001) 1727–1738.
[55] GB/T 13083-2002, Determination of fluorine in feed-Ion selective electrode method, CN-GB.
[56] O. Benali, M. Abdelmoula, J.M.R. Génin, Effect of Phosphate on the Oxidation of Hydroxysulfate Green Rust 765 (2005) 85–90.
[57] X. Zhao, Y.L. Wang, J.L. Guo, Modification of the micro-interface adsorption model on particles with fractal theory-Langmuir, Freundlich and surface complexation adsorption model, Acta Scientiae Circumstantiae 25 (2005) 52–57.
[58] C.S. Sundaram, N. Viswanathan, S. Meenakshi, Defluoridation chemistry of synthetic hydroxyapatite at nano scale: equilibrium and kinetic studies, J. Hazard. Mater. 155 (2008) 206–215.
[59] Chang-Jing Li, Z.-D. Wei, Groundwater Quality and Pollution, China Architecture & Building Press, Beijing, 1983.
[60] L. Chai, Y. Wang, N. Zhao, W. Yang, X. You, Sulfate-doped Fe_3O_4/Al_2O_3 nanoparticles as a novel adsorbent for fluoride removal from drinking water, Water Res. 47 (2013) 4040–4049.
[61] K. Babaeivelni, A.P. Khodadoust, Adsorption of fluoride onto crystalline titanium dioxide: effect of pH, ionic strength, and co-existing ions, J. Colloids Interface Sci. 394 (2013) 419–427.
[62] C.F. Chang, C.Y. Chang, T.L. Hsu, Removal of fluoride from aqueous solution with the superparamagnetic zirconia material, Desalination 279 (2011) 375–382.
[63] X. Zhao, J. Wang, F. Wu, T. Wang, Y. Cai, Y. Shi, G. Jiang, Removal of fluoride from aqueous media by Fe_3O_4@$Al(OH)_3$ magnetic nanoparticles, J. Hazard. Mater. 173 (2010) 102–109.
[64] N. Thakur, S.A. Kumar, H. Parab, A.K. Pandey, P. Bhatt, S.D. Kumar, A.V.R. Reddy, A fluoride ion selective Zr(IV)-poly(acrylamide) magnetic composite, RSC Adv. 4 (2014) 10350.
[65] P.K. Raul, R.R. Devi, I.M. Umlong, S. Banerjee, L. Singh, M. Purkait, Removal of fluoride from water using iron oxide-hydroxide nanoparticles, J. Nanosci. Nanotechnol. 12 (2012) 3922–3930.
[66] N. Papassiopi, K. Vaxevanidou, C. Christou, E. Karagianni, G.S. Antipas, Synthesis, characterization and stability of Cr(III) and Fe(III) hydroxides, J. Hazard. Mater. 264 (2014) 490–497.